J. Phys. Chem. A **2005,** *109,* 1675−1683

Analysis of the Effect of Spin−Orbit Coupling on the Electronic Structure and Excitation Spectrum of the Bi_2^{2-} Anion in $(K\text{-crypt})_2Bi_2$ on the Basis of Relativistic Electronic Structure Calculations

Dadi Dai and Myung-Hwan Whangbo*

Department of Chemistry, North Carolina State University, Raleigh, North Carolina 27695-8204

Angel Ugrinov and Slavi C. Sevov*

Department of Chemistry and Biochemistry, University of Notre Dame, Notre Dame, Indiana 46556

Fan Wang[†] and Lemin Li*

Department of Chemistry, Peking University, Beijing 100871, The People's Republic of China

Antoine Villesuzanne*

ICMCB-CNRS, 87, avenue du Dr. A. Schweitzer, 33608 Pessac Cedex, France

Aleksey B. Alekseyev,* Heinz-Peter Liebermann, and Robert J. Buenker*

Bergische Universität Wuppertal, Fachbereich C -Theoretische Chemie, Gaussstrasse 20,
D-42097 Wuppertal, Germany

Received: November 22, 2004

The Bi_2^{2-} anions that have been characterized in $(K\text{-crypt})_2Bi_2$ are isoelectronic with O_2 but are diamagnetic and EPR-silent, unlike O_2. The UV−vis spectrum measured for $(K\text{-crypt})_2Bi_2$ shows two broad absorption peaks located at 2.05 and 2.85 eV, but no absorption at lower energies down to 0.62 eV. To account for these observations, the electronic structures of the isoelectronic diatomic dianions Q_2^{2-} (Q = N, P, As, Sb, Bi) were compared on the basis of relativistic density functional theory calculations, and the electronic excitations of Bi_2^{2-} were analyzed on the basis of relativistic configuration interaction calculations. The extent of spin−orbit coupling, brought about by the relativistic effect, increases steadily in the order N < P < As < Sb < Bi such that the "closed-shell" state is more stable than the "open-shell" state for Bi_2^{2-}, while the opposite is the case for N_2^{2-}, P_2^{2-}, As_2^{2-}, and Sb_2^{2-}. The nature of the electronic excitations of Bi_2^{2-} was assigned and discussed from the viewpoint of molecular orbitals in the absence of spin−orbit coupling.

1. Introduction

Molecular orbital (MO) pictures provide a useful framework of thinking about the electronic structures of a variety of molecules. Nevertheless, they often become inadequate for molecules made up of heavy elements. For example, the paramagnetism of O_2 is readily explained in terms of its triplet ground state, since there are only two electrons to fill its doubly degenerate HOMO (i.e., the pi-antibonding orbitals, π^*). By analogy, a dianion Bi_2^{2-} that is isoelectronic with O_2 would have been expected to possess a similar electronic structure and exhibit paramagnetism. First principles electronic structure calculations using relativistic effective-core potentials confirmed this expectation.[1] However, the Bi_2^{2-} anions characterized in $(K\text{-crypt})_2Bi_2$ show diamagnetic properties (here crypt refers to 4,7,13,16,21,24-hexaoxa-1,10-diazabicyclo[8.8.8]hexacosane). $(K\text{-crypt})_2Bi_2$ exhibits negative and temperature-independent magnetic susceptibility in the range 10−300 K and is EPR-silent at room and liquid nitrogen temperatures.[1,2] Therefore, unlike paramagnetic O_2, the Bi_2^{2-} anions of $(K\text{-crypt})_2Bi_2$ behave as if their ground state is "singlet" with no unpaired electrons. It is well known that relativistic effects in heavy atoms lead to a very strong spin−orbit coupling and can exert a profound influence on the chemical bonding of compounds involving such elements.[3−21] Indeed, it has been pointed out that paramagnetic effects can be largely suppressed when spin−orbit coupling becomes large compared to thermal energy.[4] The ground state of neutral diatomic molecule Bi_2 has been examined by electronic structure calculations including spin−orbit coupling within Hartree−Fock[14−16] and DFT schemes.[17−21] In describing the valence electronic structure of a diatomic species such as Bi_2^{2-}, it is necessary to consider spin−orbit coupling explicitly for valence electrons. Furthermore, the UV−vis spectrum determined for $(K\text{-crypt})_2Bi_2$ in ethylenediamine solution at room temperature shows two broad absorption peaks located at 2.05 and 2.85 eV, but no absorption peaks at lower energies down to 0.62 eV (see below). The electronic excitations responsible for this observation are not well understood.

In the present work we examine how the increase in spin−orbit coupling affects the valence electronic structures of the isoelectronic diatomic dianions Q_2^{2-} (Q = N, P, As, Sb, Bi) on

---

* Corresponding authors.

[†] Present address: Department of Chemistry, University of Calgary, Calgary, Alberta, Canada T2N 1N4.

10.1021/jp044675q CCC: $30.25

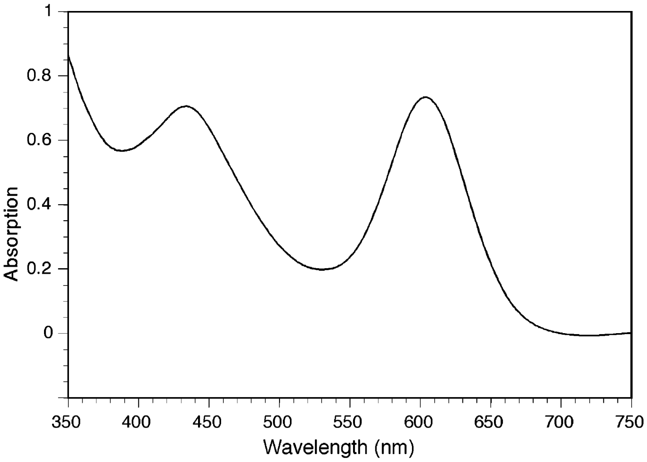

Figure 1. UV−vis spectrum of (K-crypt)$_2$Bi$_2$ in ethylenediamine at room temperature. The peaks are located at 435 nm (2.85 eV) and 605 nm (2.05 eV).

the basis of relativistic density functional theory (DFT) calculations, analyze the electronic excitations of Bi$_2^{2-}$ on the basis of relativistic configuration interaction (CI) calculations and interpret the UV−vis spectrum determined for (K-crypt)$_2$Bi$_2$ in ethylenediamine solution. Our work is organized as follows. Section 2 briefly summarizes the synthesis and physical properties of (K-crypt)$_2$Bi$_2$, and section 3 our relativistic DFT and CI calculations for an isolated Bi$_2^{2-}$ anion. The nature of the ground state of Bi$_2^{2-}$ is discussed in section 4 on the basis of the relativistic DFT calculations. In section 5 we discuss on the basis of the relativistic DFT calculations the nature of the one-electron orbitals of Bi$_2^{2-}$ as well as the electronic excitations expected for Bi$_2^{2-}$. In section 6 we describe results of our relativistic CI calculations for Bi$_2^{2-}$, assign the electronic excitation spectrum of (K-crypt)$_2$Bi$_2$, and discuss briefly why the present relativistic DFT calculations are inadequate for describing electronic excitations. Our main conclusions are summarized in section 7.

2. Experimental Section

(K-crypt)$_2$Bi$_2$ was synthesized from the precursor K$_3$Bi$_2$ as described before.[1,2] Its UV−vis spectrum (Figure 1) in ethylenediamine was taken at room temperature on a Perkin-Elmer UV/VIS/NIR spectrometer Lambda 19 in the range 250−2000 nm (i.e., 4.96−0.62 eV). It shows two peaks at 435 and 605 nm (Figure 1) and no absorption peaks at lower energies down to 0.62 eV. At energies below 0.62 eV, the spectrum is very complex due to the presence of solvent molecules, ethylenediamine, and large organic molecules such as 2,2,2-crypt. This makes it impossible to draw any meaningful conclusion about the electronic excitations of the Bi$_2^{2-}$ anion below 0.62 eV.

The magnetization of 11 mg of (K-crypt)$_2$Bi$_2$ was measured at a field of 3T over the range 10−300 K on a Quantum Design MPMS SQUID magnetometer. The results show negative and temperature independent magnetic susceptibility varying in the range of (-1.3 to -2.7) $\times 10^{-4}$ emu/mol. The measurements were carried out in a special holder designed for air-sensitive compounds where the sample is confined between two quartz rods that are tightly fitted in a sealed quartz tube. EPR measurements of ethylenediamine solutions of the compound were carried out on a Varian EC-1365E spectrometer at both room and liquid-nitrogen temperatures and showed that the compound is EPR silent. All operations were carried out in a nitrogen-filled glovebox with moisture level below 1 ppm.

3. Relativistic Electronic Structure Computations

3.1. DFT Calculations. The Beijing density function program[22,23] was used for our four-component fully relativistic DFT calculations for Q$_2^{2-}$ (Q = N, P, As, Sb, Bi). The 2s/2p orbitals of N, the 3s/3p orbitals of P, the 4s/4p/3d orbitals of As, the 5s/5p/4d orbitals of Sb, and the 6s/6p/5d orbitals of Bi are considered as valence shells, while other orbitals are frozen in the core. The Becke88 [24] and Perdew86 [25] functionals were selected as the exchange-correlation functionals. For the calculations of the orbital energies of Q$_2^{2-}$, the Q−Q bond lengths of Q$_2^{2-}$ were optimized by minimizing their total electronic energies. For the calculations of the excitation energies of Bi$_2^{2-}$, the Bi−Bi bond length was set to the experimental value (i.e., 2.8377 Å) found for (K-crypt)$_2$Bi$_2$. The Kramers unrestricted scheme was used to treat the open-shell systems.[23]

3.2. CI Calculations. To analyze the UV−vis spectrum of (K-crypt)$_2$Bi$_2$ in more detail, a series of relativistic CI calculations were carried out for Bi$_2^{2-}$. For this purpose, a relativistic effective core potential of Wildman et al.[26] was employed to describe the inner-shell electrons of the bismuth atom, and the 5d, 6s, and 6p electrons were treated as valence electrons. We employed the (6s6p6d1f)/[4s4p4d1f] atomic orbital basis set for Bi,[26] which was augmented by one more f function with an optimized exponent of 0.12.

In our relativistic CI calculations two different computational methods were adopted. In the first approach, a self-consistent field (SCF) calculation was combined with a large scale CI to obtain highly correlated Λ-S wave functions in the absence of spin−orbit coupling. As a next step a spin−orbit matrix for a relatively small number of Λ-S states (≤ 100) was diagonalized to obtain energies and wave functions for the final Ω states. Thus, this approach is characterized as Λ-S contracted spin−orbit CI (LSC−SO−CI) calculations. In the second approach, we treated the electrostatic and spin−orbit interactions simultaneously without first obtaining correlated Λ-S functions, so that all selected configurations of various space and spin symmetries form the basis for the multireference spin−orbit CI (MR−SO−CI) calculations. The MR−SO−CI method is computationally much more demanding than the LSC−SO−CI method. More details for both methods were described elsewhere.[27,28]

The standard multireference single- and double-excitation CI approach [29] was used to obtain the Λ-S electronic energies, wave functions and transition moments. The calculations were carried out employing the Table Direct-CI [30,31] version of the MRD-CI package including configuration selection and perturbative corrections. The MO's that are predominantly occupied by the 5d^{10} electrons were frozen at the CI stage of the calculations. A selection threshold of $T = 0.3 \times 10^{-6}$ E_h was used in the LSC−SO−CI and MR−SO−CI methods. In the LSC−SO−CI scheme, eight to twelve lowest roots were calculated for each of all possible singlet and triplet irreducible representations, and typical sizes of the selected CI spaces were $1.8-3.2 \times 10^5$ in each case. Quintet states are less important for the low-energy Bi$_2^{2-}$ spectrum, and only two to four roots were obtained for them, with CI spaces varying from 80 000 to 120 000 selected configurations, depending on symmetry. The importance of higher excitations in the LSC−SO−CI treatment were assessed by applying the generalized multireference analogue of the Davidson correction[32,33] to the extrapolated $T = 0$ energies of each root. There is a good overall agreement between the data computed in the LSC−SO−CI and MR−SO−CI approaches (see section 6). However, in the MR−SO−CI method, all configurations that have strong coupling with the states of

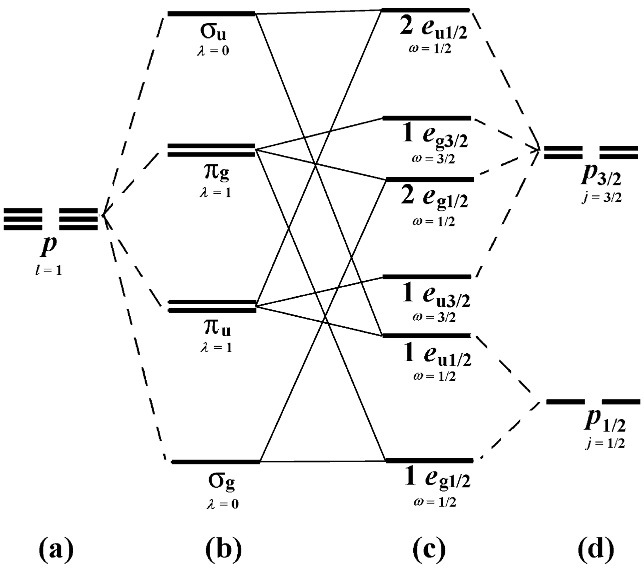

Figure 2. One-electron energy levels of a homonuclear diatomic dianion Q_2^{2-} (Q = N, P, As, Sb, Bi) derived primarily from the valence p orbitals of Q: (a) The p orbitals of two Q atoms without considering spin−orbital coupling, (b) the molecular orbitals of Q_2^{2-} formed from the p orbitals without considering spin−orbital coupling, (c) the relativistic dimer levels of Q_2^{2-} formed from the p orbitals under spin−orbit coupling, and (d) the p orbitals of two Q atoms under spin−orbit coupling. The one-electron energy levels of Q_2^{2-} derived mainly from the valence s orbitals of Q, which lie below the p-block levels described above, are not shown, and the slight mixing between the s- and p-block levels is neglected for simplicity.

interest can be directly included in the secular matrix to be diagonalized. The latter is particularly important for systems containing very heavy atoms such as Bi. This suggests that the MR−SO−CI approach would be more accurate in the present case.

4. Nature of the Electronic Ground State

4.1. Atomic and Dimer Orbitals. When spin−orbit coupling is neglected, all the p orbitals of each atom are degenerate (Figure 2a). (For simplicity of our discussion, we describe only the valence p orbitals of each atom Q.) Once a diatomic molecule is formed, the spherical symmetry of the individual atoms is lowered to cylindrical symmetry, and thus only the angular momentum pointed along the inter-nuclear axis is meaningful. The orbital angular momentum of a diatomic molecule along the inter-nuclear axis is designated by λ, analogous to the l quantum number for an electron of an atom: $\lambda = 0$ for σ-type orbitals, and $\lambda = 1$ for π-type orbitals (Figure 2b).

The coupling of the spin angular momentum s and the angular momentum λ leads to a net angular momentum, which is analogous to the j angular momentum for an electron of an atom. The resulting angular momentum is denoted by ω. For example, $\omega = |\lambda \pm 1/2|$ for a spin-1/2 electron. As a consequence, under spin−orbit coupling, the σ ($\lambda = 0$) level becomes the $\omega = 1/2$ level, whereas the π ($\lambda = 1$) level splits into the $\omega = 1/2$ and $\omega = 3/2$ levels. Because the z-component of ω (i.e., m_ω) is given by $m_\omega = \pm\omega$ by the cylindrical symmetry, each relativistic dimer orbital is 2-fold degenerate and hence will be denoted by the symbol e. The relativistic dimer levels resulting from the p orbitals under spin−orbit coupling are depicted in Figure 2c. The occurrence of these levels is easily accounted for by introducing spin−orbit coupling first into the p orbitals of an atom to split them into $p_{1/2}$ ($j = 1/2$, $m_j = \pm1/2$) and $p_{3/2}$ ($j = 3/2$, $m_j = \pm1/2, \pm3/2$) (Figure 2d). Then the $p_{1/2}$ orbitals of the two individual atoms interact to form the $e_{g1/2}$ and $e_{u1/2}$ orbitals. Likewise, the $p_{3/2}$ orbitals interact to form the $e_{g1/2}$, $e_{u1/2}$, $e_{g3/2}$, and $e_{u3/2}$ orbitals (Figure 2d to 2c). The correlations between the MO levels of Figure 2b and the relativistic dimer levels of Figure 2c, indicated by the solid lines, are discussed in section 5.2.

TABLE 1: Results of Relativistic DFT Calculations for Q_2^{2-} (Q = N, P, As, Sb, Bi)[a]

		N_2^{2-}	P_2^{2-}	As_2^{2-}	Sb_2^{2-}	Bi_2^{2-}
$\epsilon(p_{3/2}) - \epsilon(p_{1/2})$[a]		0.019	0.055	0.282	0.632	1.969
$\epsilon(1e_{g3/2}) - \epsilon(2e_{g1/2})$[a,b]		0.01	0.03	0.14	0.25	0.57
$(E_{OS} - E_{CS})$[a,c]		−0.88	−0.46	−0.30	−0.11	+0.26
Q−Q lengths[d]	OS	1.3664	2.1528	2.4044	2.7951	3.0101
	CS	1.3658	1.1584	2.4121	2.8109	3.0199

[a] The energies are given in eV units. [b] The energies were calculated by using the CS states with the optimized bond lengths. [c] The energies were calculated by using the optimized bond lengths. [d] The optimized bond lengths are given in Å units.

4.2. Ground State. For Q_2^{2-} (Q = N, P, As, Sb, Bi), there remain two electrons for the $2e_{g1/2}$, $1e_{g3/2}$ and $2e_{u1/2}$ levels after completely filling all the levels up to $1e_{u3/2}$. The energy gap between $2e_{g1/2}$ and $1e_{g3/2}$ is small when spin−orbit coupling is weak, and increases as spin−orbit coupling becomes stronger. Thus, there are two low-energy electron configurations to consider, $(2e_{g1/2})^2(1e_{g3/2})^0$ and $(2e_{g1/2})^1(1e_{g3/2})^1$. (Unless mentioned otherwise, it will be assumed that all levels below $2e_{g1/2}$ are each doubly filled.) The terms "singlet" and "triplet" states are valid concepts in MO pictures where spin−orbit coupling is neglected. However, these states can interact and mix when spin−orbit coupling is turned on. Thus, it is more appropriate to describe the $(2e_{g1/2})^2(1e_{g3/2})^0$ configuration as a "closed-shell" (CS) state, and $(2e_{g1/2})^1(1e_{g3/2})^1$ as an "open-shell" (OS) state.

The computational results for Q_2^{2-}, summarized in Table 1, indicate that the energy gap between the $2e_{g1/2}$ and $1e_{g3/2}$ levels is large for strong spin−orbit coupling, and the CS state becomes more stable than the OS state.[34] The energy difference between the $p_{3/2}$ and $p_{1/2}$ levels of Q increases in the order N < P < As < Sb < Bi, and so does the energy difference between the $2e_{g1/2}$ and $1e_{g3/2}$ levels of Q_2^{2-}. The state energy difference, $\Delta E = E_{OS} - E_{CS}$, is largest for N_2^{2-} and decreases steadily in the order N > P > As > Sb > Bi. The OS state is more stable than the CS state for N_2^{2-}, P_2^{2-}, As_2^{2-} and Sb_2^{2-}, but the opposite is the case for Bi_2^{2-}. The latter explains why the Bi_2^{2-} anions of (K-crypt)$_2$Bi$_2$ behave as if they have no unpaired electrons in contrast to the case of the isoelectronic O_2.[1,2]

It is noted that the optimized bond length of the CS state Bi_2^{2-}, 3.0101 Å, is longer than the experimental value, 2.8377 Å. The exchange and correlation functionals used here tend to slightly overestimate bond lengths.[20] Furthermore, our calculations were carried out for an isolated Bi_2^{2-} anion, whereas the Bi_2^{2-} anions in the crystal structure of (K-crypt)$_2$Bi$_2$ are coordinated with the counterbalancing cations K^+. The polarization of the valence electron density distribution of Bi_2^{2-} by the surrounding K^+ cations will effectively reduce the electrostatic repulsion between the two Bi atoms and hence shorten the Bi−Bi bond length. In addition, we note that the effective core potential used has a large core. The omission of the outer core might also have contributed to the long Bi−Bi bond length optimized from the present DFT calculations.[35]

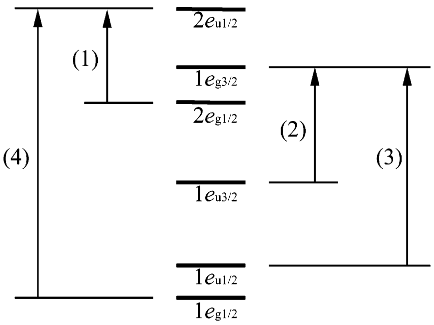

Figure 3. Four low-energy electronic excitations of Bi_2^{2-}.

TABLE 2: Compositions of the Ground and Four Excited Configurations of Bi_2^{2-} and the Associated Excitation Energies Obtained by Relativistic DFT Calculations

state	composition	excitation energy (eV)[a]
$(2e_{g1/2})^2(1e_{g3/2})^0$	0_g^+	
$(2e_{g1/2})^1(2e_{u1/2})^1$	0_u^+, 0_u^-, 1_u	0.90
$(1e_{u3/2})^1(1e_{g3/2})^1$	0_u^+, 0_u^-, 3_u	1.17
$(1e_{u1/2})^1(1e_{g3/2})^1$	1_u, 2_u	2.21
$(1e_{g1/2})^1(2e_{u1/2})^1$	0_u^+, 0_u^-, 1_u	3.11

[a] Calculated for Bi_2^{2-} with the Bi−Bi distance 2.8377 Å found in (K-crypt)$_2$Bi$_2$.

5. Excitation Spectrum of Bi_2^{2-} from the Viewpoint of One-Electron Orbitals

5.1. DFT Calculations of the Excitation Energies. In the CS state of Bi_2^{2-} represented by the orbitals of Figure 2c, the $1e_{g1/2}$, $1e_{u1/2}$, $1e_{u3/2}$, and $2e_{g1/2}$ levels, are doubly filled while the $1e_{g3/2}$ and $2e_{u1/2}$ levels are empty. Electronic excitations are allowed between occupied u- and unoccupied g-levels, and between occupied g- and unoccupied u-levels. Figure 3 depicts four low-energy one-electron excitations: (1) $2e_{g1/2} \rightarrow 2e_{u1/2}$, (2) $1e_{u3/2} \rightarrow 1e_{g3/2}$, (3) $1e_{u1/2} \rightarrow 1e_{g3/2}$, and (4) $1e_{g1/2} \rightarrow 2e_{u1/2}$. We calculated the energies of these excitations for Bi_2^{2-} with Bi−Bi distance of 2.8377 Å on the basis of relativistic DFT using Slater's transition state technique (Table 2).[36−38] This method excludes the possibility of transitions between empty levels (e.g., $1e_{g3/2} \rightarrow 2e_{u1/2}$) from contributing to the excitation energy spectrum because both levels are unoccupied in the ground state.

Relativistic DFT calculations are based on the single-determinant method, so that each excitation energy determined by these calculations represents an "average" value that involves several states from the viewpoint of the CI method. Therefore, it is necessary to examine the compositions of the ground and four excited states. The ground-state configuration $(2e_{g1/2})^2(1e_{g3/2})^0$ has the 0_g^+ symmetry under the classification of relativistic states under cylindrical symmetry. According to the $\omega-\omega$ coupling scheme, the coupling of ω_1 and ω_2 states yields $\Omega = |\omega_1-\omega_2|$ and $\omega_1+\omega_2$ states. Thus, the coupling of $\omega_1=1/2$ and $\omega_2=1/2$ states generates $\Omega = 0^+$, 0^-, and 1 states.[39] Therefore, the excited configurations $(2e_{g1/2})^1(2e_{u1/2})^1$ and $(1e_{g1/2})^1(2e_{u1/2})^1$ generate 0_u^+, 0_u^-, and 1_u states. Similarly, the coupling of $\omega_1=1/2$ and $\omega_2=3/2$ states leads to $\Omega = 1$ and 2 states, so the excited configuration $(1e_{u1/2})^1(1e_{g3/2})^1$ generates 1_u and 2_u states. The coupling of $\omega_1=3/2$ and $\omega_2=3/2$ states leads to $\Omega = 0^+$, 0^-, and 3, so the excited configuration $(1e_{u3/2})^1(1e_{g3/2})^1$ generates 0_u^+, 0_u^-, and 3_u states.

According to the selection rules for electronic transitions between relativistic states under cylindrical symmetry, the $0_g^+ \rightarrow 0_u^+$ and $0_g^+ \rightarrow 1_u$ excitations are allowed, whereas the $0_g^+ \rightarrow 0_u^-$, $0_g^+ \rightarrow 2_u$, and $0_g^+ \rightarrow 3_u$ excitations are forbidden. Therefore, all four excitations of Figure 3, i.e., $2e_{g1/2} \rightarrow 2e_{u1/2}$, $1e_{u3/2} \rightarrow 1e_{g3/2}$, $1e_{u1/2} \rightarrow 1e_{g3/2}$, and $1e_{g1/2} \rightarrow 2e_{u1/2}$, are allowed. Thus it is tempting to suggest that the two absorption peaks at 2.05 and 2.85 eV (Figure 1) in the UV−vis spectrum of (K-crypt)$_2$Bi$_2$ are associated with the excitations $1e_{u1/2} \rightarrow 1e_{g3/2}$ (2.21 eV) and $1e_{g1/2} \rightarrow 2e_{u1/2}$ (3.11 eV), respectively, and that the remaining two predicted excitations, i.e., $2e_{g1/2} \rightarrow 2e_{u1/2}$ (0.90 eV) and $1e_{u3/2} \rightarrow 1e_{g3/2}$ (1.17 eV) are not observed experimentally because their transition probabilities are very small. However, this reasoning is incorrect, as discussed in the following.

5.2. Relativistic Orbitals in Terms of Nonrelativistic Orbitals. In relativistic theory an atomic orbital is represented by four components, two large components and two small components. For simplicity, we will consider only the two large components of an atomic orbital. Then, the atomic $p_{1/2}$ and $p_{3/2}$ orbitals (for positive m_s values) of Bi are written as[3]

$$p_{1/2}\ (m_s = 1/2):\quad \phi_a \propto \begin{bmatrix} -\sqrt{1/3}p_z \\ -\sqrt{1/3}(p_x + ip_y) \end{bmatrix} \tag{1a}$$

$$p_{3/2}\ (m_s=3/2):\quad \phi_b \propto \begin{bmatrix} \sqrt{1/2}(p_x + ip_y) \\ 0 \end{bmatrix} \tag{1b}$$

$$p_{3/2}\ (m_s = 1/2):\quad \phi_c \propto \begin{bmatrix} \sqrt{2/3}p_z \\ -\sqrt{1/6}(p_x + ip_y) \end{bmatrix} \tag{1c}$$

where the p_x, p_y, and p_z are the p orbitals of Bi in the absence of spin−orbit coupling, and the z-axis taken along the Bi−Bi axis.

To understand the nature of the dimer orbitals under spin−orbit coupling (Figure 2c), we first consider "equal-weight" linear combinations of the relativistic atomic orbitals ϕ_a, ϕ_b, and ϕ_c listed in eq 1. The two different Bi atoms of a Bi_2^{2-} anion may be distinguished by the site indices 1 and 2. Then,

$$\phi_a(1) + \phi_a(2) = \begin{bmatrix} -\sqrt{1/3}\sigma_z^* \\ -\sqrt{1/3}(\pi_x + i\pi_y) \end{bmatrix} \tag{2a}$$

$$\phi_a(1) - \phi_a(2) = \begin{bmatrix} -\sqrt{1/3}\sigma_z \\ -\sqrt{1/3}(\pi_x^* + i\pi_y^*) \end{bmatrix} \tag{2b}$$

$$\phi_b(1) + \phi_b(2) = \begin{bmatrix} \sqrt{1/2}(\pi_x + i\pi_y) \\ 0 \end{bmatrix} \tag{2c}$$

$$\phi_b(1) - \phi_b(2) = \begin{bmatrix} \sqrt{1/2}(\pi_x^* + i\pi_y^*) \\ 0 \end{bmatrix} \tag{2d}$$

$$\phi_c(1) + \phi_c(2) = \begin{bmatrix} \sqrt{2/3}\sigma_z^* \\ -\sqrt{1/6}(\pi_x + i\pi_y) \end{bmatrix} \tag{2e}$$

$$\phi_c(1) - \phi_c(2) = \begin{bmatrix} \sqrt{2/3}\sigma_z \\ -\sqrt{1/6}(\pi_x^* + i\pi_y^*) \end{bmatrix} \tag{2f}$$

where σ represents the sigma-bonding orbital σ_g, and σ* the sigma-antibonding orbital σ_u, in the absence of spin−orbit coupling. Likewise, π represents the pi-bonding orbital π_u, and π* the pi-antibonding orbital π_g, in the absence of spin−orbit coupling. The six dimer orbitals of a Bi_2^{2-} anion under spin−orbit coupling (Figure 2c) can be decomposed in terms of the orbitals listed in eq 2. Results of this analysis are summarized in Table 3. On the basis of eq 2 and Table 3, it is straightforward to establish the correlations between the MO levels of Figure

TABLE 3: Major and Minor Components of the Six Levels $1e_{g1/2}$, $1e_{u1/2}$, $1e_{u3/2}$, $2e_{g1/2}$, $1e_{g3/2}$, and $2e_{u1/2}$ of Bi_2^{2-} Obtained from Relativistic DFT Calculations

	major component	minor component
$1e_{g1/2}$	$\phi_a(1) - \phi_a(2)$	$\phi_c(1) - \phi_c(2)$
$1e_{u1/2}$	$\phi_a(1) + \phi_a(2)$	$\phi_c(1) + \phi_c(2)$
$1e_{u3/2}$	$\phi_b(1) + \phi_b(2)$	
$2e_{g1/2}$	$\phi_c(1) - \phi_c(2)$	$\phi_a(1) - \phi_a(2)$
$1e_{g3/2}$	$\phi_b(1) - \phi_b(2)$	
$2e_{u1/2}$	$\phi_c(1) + \phi_c(2)$	$\phi_a(1) + \phi_a(2)$

2b and the relativistic dimer levels of Figure 2c as indicated by the solid lines.

The relativistic $1e_{g1/2}$ and $2e_{g1/2}$ levels consist mainly of the $[\phi_a(1) - \phi_a(2)]$ and $[\phi_c(1) - \phi_c(2)]$ orbitals, which are made up of the σ and π^* MO character (eqs 2b and 2f). Likewise, the relativistic $1e_{u1/2}$ and $2e_{u1/2}$ levels consist mainly of the $[\phi_a(1) + \phi_a(2)]$ and $[\phi_c(1) + \phi_c(2)]$ orbitals, which are made up of the σ^* and π MO character (eqs 2a and 2e). In other words, the spin−orbit coupling induces the mixing of the sigma-bonding and the pi-antibonding MO character, and that of the sigma-antibonding and the pi-bonding MO character. It is of interest to see how this orbital mixing comes about. Under spin−orbit coupling, the σ and σ^* ($\lambda = 0$) levels become $\omega = 1/2$ levels, whereas the π and π^* ($\lambda = 1$) levels split into $\omega = 1/2$ and $\omega = 3/2$ levels. The levels of an identical ω value can interact and hence mix together, but the resulting dimer orbitals must be either gerade or ungerade in symmetry. Thus, the gerade $\omega = 1/2$ levels combine σ and π^* orbitals (eqs 2b and 2f), while the ungerade $\omega = 1/2$ levels combine σ^* and π orbitals (eqs 2a and 2e). The σ and σ^* orbitals with $\omega = 1/2$ do not mix due to their difference in symmetry. For the same reason, the π and π^* orbitals with $\omega = 3/2$ do not mix (eqs 2c and 2d). When the spin−orbit coupling is strong, the quantum number λ is not a good quantum number any more, so that the MO terms such as the sigma and pi bonding/antibonding levels become meaningless.

5.3. Consideration of Transition Dipole Moments. The probability P of the electronic excitation from a filled orbital ϕ_i to an empty orbital ϕ_f is given by $P \propto |\langle\phi_i|\vec{M}|\phi_f\rangle|^2$, where $\vec{M} = e\vec{r}$. In this section, we evaluate the transition dipole moment $\langle\phi_i|\vec{M}|\phi_f\rangle$ for the four transitions $2e_{g1/2} \rightarrow 2e_{u1/2}$, $1e_{u3/2} \rightarrow 1e_{g3/2}$, $1e_{u1/2} \rightarrow 1e_{g3/2}$, and $1e_{g1/2} \rightarrow 2e_{u1/2}$. To simplify our discussion, we note from Table 3 that the major components of the six dimer orbitals are given by

$$
\begin{aligned}
1e_{g1/2} &\leftarrow \phi_a(1) - \phi_a(2)\\
1e_{u1/2} &\leftarrow \phi_a(1) + \phi_a(2)\\
1e_{u3/2} &\leftarrow \phi_b(1) + \phi_b(2)\\
2e_{g1/2} &\leftarrow \phi_c(1) - \phi_c(2)\\
1e_{g3/2} &\leftarrow \phi_b(1) - \phi_b(2)\\
2e_{u1/2} &\leftarrow \phi_c(1) + \phi_c(2)
\end{aligned} \tag{3}
$$

Using only these major components, the transition dipole moments associated with the four electronic excitations are written as

$$
\begin{aligned}
\langle 2e_{g1/2}|\vec{M}|2e_{u1/2}\rangle &\propto (2/3)\,\langle\sigma_z|\vec{r}\,|\sigma_z^*\rangle + (1/3)\,\langle\pi_x^*|\vec{r}\,|\pi_x\rangle\\
\langle 1e_{u3/2}|\vec{M}|1e_{g3/2}\rangle &\propto \langle\pi_x|\vec{r}\,|\pi_x^*\rangle = \langle\pi_x^*|\vec{r}\,|\pi_x\rangle\\
\langle 1e_{u1/2}|\vec{M}|1e_{g3/2}\rangle &\propto \sqrt{1/6}(1 + i)\,\langle\sigma_z^*|\vec{r}\,|\pi_x^*\rangle\\
\langle 1e_{g1/2}|\vec{M}|2e_{u1/2}\rangle &\propto (\sqrt{2}/3)(-\,\langle\sigma_z|\vec{r}\,|\sigma_z^*\rangle + \langle\pi_x^*|\vec{r}\,|\pi_x\rangle)
\end{aligned} \tag{4}
$$

where the equivalence between $\langle\pi_x^*|\vec{r}|\pi_x\rangle$ and $\langle\pi_x^*|\vec{r}|\pi_y\rangle$ was taken into consideration, and so was that between $\langle\sigma_z^*|\vec{r}|\pi_x^*\rangle$ and $\langle\sigma_z^*|\vec{r}|\pi_y^*\rangle$. By symmetry, the nonzero term of $\langle\sigma_z|\vec{r}|\sigma_z^*\rangle$ is given by $\langle\sigma_z|z|\sigma_z^*\rangle$, that of $\langle\pi_x^*|\vec{r}|\pi_x\rangle$ by $\langle\pi_x^*|z|\pi_x\rangle$, and that of $\langle\sigma_z^*|\vec{r}|\pi_x^*\rangle$ by $\langle\sigma_z^*|x|\pi_x^*\rangle$. Therefore, eq 4 is simplified as

$$
\begin{aligned}
\langle 2e_{g1/2}|\vec{M}|2e_{u1/2}\rangle &\propto (2/3)\,\langle\sigma_z|z|\sigma_z^*\rangle + (1/3)\,\langle\pi_x^*|z|\pi_x\rangle\\
\langle 1e_{u3/2}|\vec{M}|1e_{g3/2}\rangle &\propto \langle\pi_x^*|z|\pi_x\rangle\\
\langle 1e_{u1/2}|\vec{M}|1e_{g3/2}\rangle &\propto \sqrt{1/6}(1 + i)\,\langle\sigma_z^*|x|\pi_x^*\rangle\\
\langle 1e_{g1/2}|\vec{M}|2e_{u1/2}\rangle &\propto (\sqrt{2}/3)(-\,\langle\sigma_z|z|\sigma_z^*\rangle + \langle\pi_x^*|z|\pi_x\rangle)
\end{aligned} \tag{5}
$$

It is important to consider whether the values of transition dipole moments such as $\langle\sigma_z|z|\sigma_z^*\rangle$, $\langle\pi_x^*|z|\pi_x\rangle$, and $\langle\sigma_z^*|x|\pi_x^*\rangle$ are large or small on symmetry considerations. Note that the term $\langle\sigma_z|z|\sigma_z^*\rangle$ is equivalent to $\langle\sigma_z|z\sigma_z^*\rangle$, i.e., the overlap integral between σ_z and $z\sigma_z^*$. Likewise, $\langle\pi_x^*|z|\pi_x\rangle$ is equivalent to $\langle\pi_x^*|z\pi_x\rangle$, and $\langle\sigma_z^*|x|\pi_x^*\rangle$ to $\langle\sigma_z^*|x\pi_x^*\rangle$. To visualize our symmetry considerations, we calculate the MO's of Bi_2^{2-} using the extended Hückel tight binding method and generate boundary surface plots of the MO's and their product functions.[40] Figure 4 presents the boundary surface density plots of the MO's σ_z and σ_z^* as well as the product functions $z\sigma_z^*$ and $\sigma_z z\sigma_z^*$. It is clear that σ_z and $z\sigma_z^*$ have the same symmetry and the regions of their large values match. Consequently, the function $\sigma_z z\sigma_z^*$ has large values so that its integrated value (i.e., $\langle\sigma_z|z|\sigma_z^*\rangle$) is expected to be large. The boundary surface plots of π_x^*, π_x, $z\pi_x$, and $\pi_x^* z\pi_x$ are shown in Figure 5. π_x^* and $z\pi_x$ have the same symmetry and the regions of their large values match, so that the $\langle\pi_x^*|z|\pi_x\rangle$ value is expected to be large. Indeed, organic conjugated molecules are known to exhibit strong absorptions due to the $\pi \rightarrow \pi^*$ transitions. Figure 6 shows the boundary surface density plots of σ_z^*, π_x^*, $x\pi_x^*$ and $\sigma_z^*\, x\, \pi_x^*$. σ_z^* and $x\pi_x^*$ do not have the same symmetry and the regions of their large values do not match. Therefore, the $\langle\sigma_z^*|x|\pi_x^*\rangle$ value is not expected to be large. In agreement with this qualitative discussion, our calculations using only the Bi 6p orbitals show that the ratio $\langle\sigma_z|z|\sigma_z^*\rangle$ to $\langle\pi_x^*|z|\pi_x\rangle$ to $\langle\sigma_z^*|x|\pi_x^*\rangle$ is 1.00:0.94:0.22. Consequently, $\langle 1e_{u3/2}|\vec{M}|1e_{g3/2}\rangle$ is large due to the large $\langle\pi_x^*|z|\pi_x\rangle$ term, while $\langle 1e_{u1/2}|\vec{M}|1e_{g3/2}\rangle$ is small due to the small $\langle\sigma_z^*|x|\pi_x^*\rangle$ term. $\langle 1e_{g1/2}|\vec{M}|2e_{u1/2}\rangle$ is small because the $\langle\sigma_z|z|\sigma_z^*\rangle$ and $\langle\pi_x^*|z|\pi_x\rangle$ terms cancel each other, but $\langle 2e_{g1/2}|\vec{M}|2e_{u1/2}\rangle$ is large because the $\langle\sigma_z|z|\sigma_z^*\rangle$ and $\langle\pi_x^*|z|\pi_x\rangle$ terms reinforce each other. The above discussion suggests that the two lower-energy excitations $2e_{g1/2} \rightarrow 2e_{u1/2}$ and $1e_{u3/2} \rightarrow 1e_{g3/2}$ should lead to strong absorptions, but the two higher-energy excitations $1e_{u1/2} \rightarrow 1e_{g3/2}$ and $1e_{g1/2} \rightarrow 2e_{u1/2}$ to weak absorptions. According to the symmetry analysis of the transition dipole moments given above, the UV−vis absorption peaks centered at 2.05 and 2.85

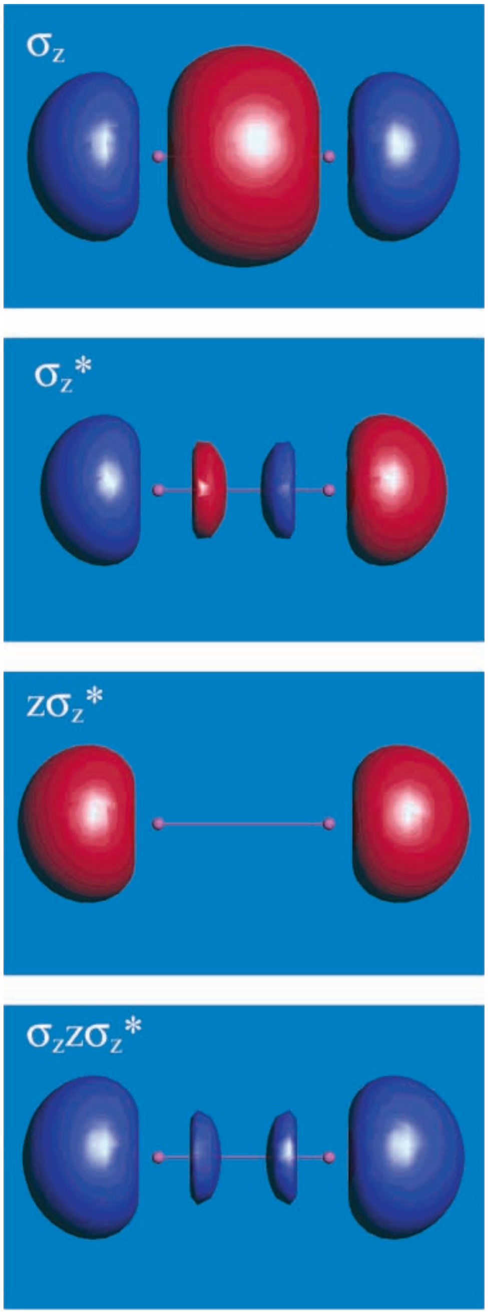

Figure 4. Boundary surface density plots of σ_z, σ_z^*, $z\sigma_z^*$, and $\sigma_z z\, \sigma_z^*$ of Bi_2^{2-} calculated for the discussion of $\langle\sigma_z|z|\sigma_z^*\rangle$. The densities used for the plots are 0.025/(au)$^{-3/2}$, 0.05/(au)$^{-3/2}$, 0.12/(au)$^{-1/2}$, and 0.003/(au)$^{-2}$ for σ_z, σ_z^*, $z\sigma_z^*$, and $\sigma_z z\, \sigma_z^*$, respectively. The positive and negative values are presented by red and blue colors, respectively. The *z*-axis is taken along the Bi−Bi axis.

eV cannot be assigned to the excitations $1e_{u1/2} \rightarrow 1e_{g3/2}$ (2.21 eV) and $1e_{g1/2} \rightarrow 2e_{u1/2}$ (3.11 eV), respectively.

6. Description of the Excitation Spectrum of Bi_2^{2-} by CI

6.1. Relative Energies of the Ground and Low-Lying Excited States. Table 4 summarizes the relative energies of the low-lying g- and u-states of Bi_2^{2-} calculated by the two CI methods at Bi−Bi = 2.910 Å (the approximate equilibrium distance of the ground state) as well as the largest Λ-S contributions to these states. The ground state $X0_g^+$ of Bi_2^{2-} has the 0_g^+ symmetry and is mainly composed of the $^3\Sigma_g^-$ and $^1\Sigma_g^+$ contributions, both dominated by the $(...\sigma_g^2\pi_u^4\pi_g^2)$ configuration, i.e., the “closed-shell” state described in section 4.2.

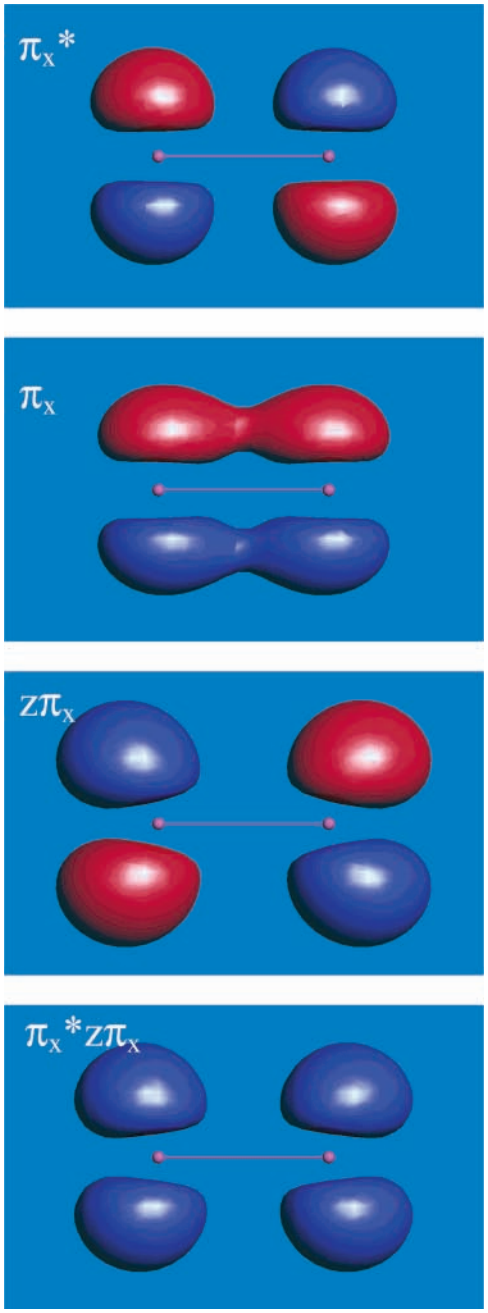

Figure 5. Boundary surface density plots of π_x^*, π_x, $z\pi_x$, and $\pi_x^* z\pi_x$ of Bi_2^{2-} calculated for the discussion of $\langle\pi_x^*|z|\pi_x\rangle$. The densities used for the plots are 0.05/(au)$^{-3/2}$, 0.05/(au)$^{-3/2}$, 0.06/(au)$^{-1/2}$, and 0.003/(au)$^{-2}$ for π_x^*, π_x, $z\pi_x$, and $\pi_x^*\, z\pi_x$, respectively.

As expected, the contribution of $^1\Sigma_g^+$ to the ground state is significantly high (∼29%) due to a strong spin−orbit interaction in Bi_2^{2-}. Accurate determination of the ground-state spectroscopic constants gives $R_e = 2.954$ Å and $\omega_e = 123$ cm^{-1}. This equilibrium Bi−Bi distance, R_e, is shorter than 3.010 Å obtained from the present DFT calculations but is still too long compared with the experimental value of 2.8377 Å (see ref 35 for further discussion).

The second lowest-lying g-state, i.e., 1_g(I), corresponds to the “open-shell” state described in section 4.2. The third low-lying g-state 2_g arises mainly from the $^1\Delta_g$ contribution with some $^3\Pi_g$ component. The next g-states lie notably higher in energy and are not discussed here because electronic transitions from the $X0_g^+$ ground state to them are forbidden. The four lowest-lying u-states are made up of the $^3\Pi_u(...\sigma_g^2\pi_u^4\pi_g\sigma_u)$

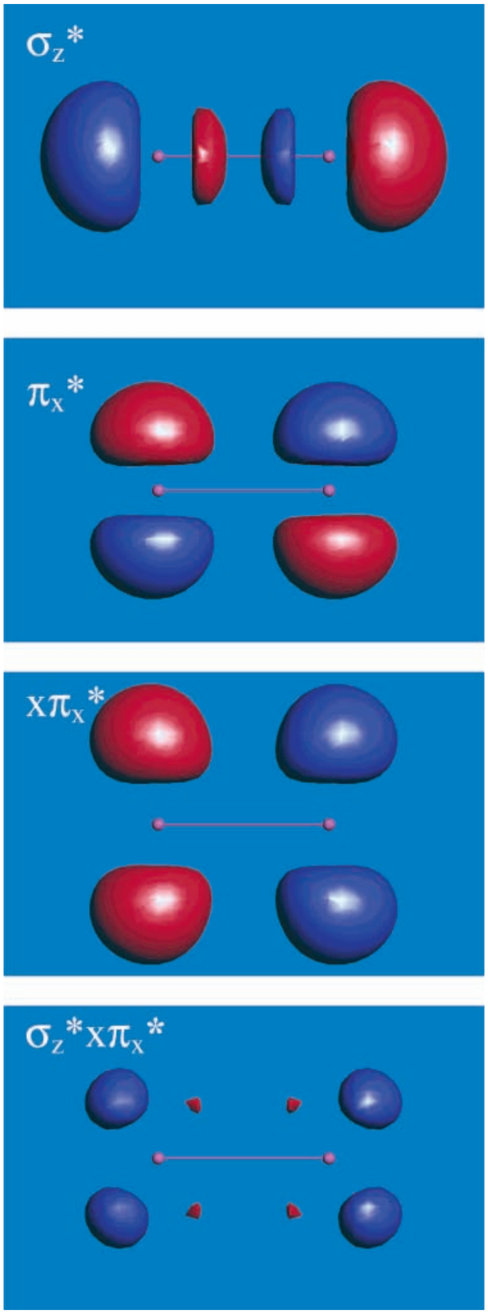

Figure 6. Boundary surface density plots of σ_z^*, π_x^*, $x\pi_x^*$, and $\sigma_z^*\ x\ \pi_x^*$ of Bi_2^{2-} calculated for the discussion of $\langle\sigma_z^*|x|\pi_x^*\rangle$. The densities used for the plots are 0.05/(au)$^{-3/2}$, 0.05/(au)$^{-3/2}$, 0.06/(au)$^{-1/2}$, and 0.003/(au)$^{-2}$ for σ_z^*, π_x^*, $x\pi_x^*$, and σ_z^* x π_x^*, respectively.

configuration. The 1_u(I) state is almost a 50/50 mixture of $^3\Pi_u$(...$\sigma_g{}^2\pi_u{}^4\pi_g\sigma_u$) and $^1\Pi_u$(...$\sigma_g{}^2\pi_u{}^4\pi_g\sigma_u$), which again shows a strong influence of the spin−orbit interaction. The 1_u(II) state is an orthogonal complement to 1_u(I). Table 4 shows that the u-states lying higher than 1_u(II) with excitation energies in the 1.0−1.6 eV range are composed of various combinations of $^{1,3}\Sigma_u{}^-$, $^{1,3}\Sigma_u{}^+$, and $^{1,3}\Delta_u$. All of these states are described mainly by two configurations $\sigma_g{}^2\pi_u{}^3\pi_g{}^3$ and $\sigma_g{}^2\pi_u{}^4\pi_g\,\pi_u^*$, and thus correspond to the $\pi_u \rightarrow \pi_g$ and $\pi_g \rightarrow \pi_u^*$ excitations from the ground state. Here the π_u^* orbital refers to the lowest-lying virtual orbital of the π_u symmetry, which is made up of the diffuse Bi p-orbitals and hence has a Rydberg character. For excitations in the electric dipole approximation, the $0_u{}^-$, 2_u, and 3_u states are not important. The $0_u{}^+$ and 1_u states of this group will be discussed in more detail below.

TABLE 4: Excitation Energies (in eV) Calculated for the 3 Lowest g-States and 13 Lowest u-States of Bi_2^{2-} Employing the LSC−SO−CI and MR−SO−CI Methods[a]

state	LSC−SO−CI	MR−SO−CI	main Λ-S contribution
$X0_g{}^+$	0	0	$^3\Sigma_g{}^-$, $^1\Sigma_g{}^+$
1_g(I)	0.37	0.35	$^3\Sigma_g{}^-$
2_g(I)	0.56	0.59	$^1\Delta_g$, $^3\Pi_g$
$0_u{}^-$(I)	0.023	0.14	$^3\Pi_u$
1_u(I)	0.054	0.15	$^3\Pi_u$, $^1\Pi_u$
$0_u{}^+$(I)	0.065	0.14	$^3\Pi_u$
2_u(I)	0.75	0.84	$^3\Pi_u$
1_u(II)	0.82	0.89	$^1\Pi_u$, $^3\Pi_u$
$0_u{}^-$(II)	1.02	1.01	1,2 $^1\Sigma^-{}_u$, 1 $^3\Sigma_u{}^+$
3_u(I)	1.06	1.06	1,2 $^3\Delta_u$
$0_u{}^-$(III)	1.45	1.42	2 $^3\Sigma_u{}^+$, 1,2 $^1\Sigma_u{}^-$
1_u(III)	1.49	1.46	1,2 $^3\Delta_u$
$0_u{}^+$(II)	1.48	1.47	1 $^3\Sigma_u{}^-$, 1 $^1\Sigma_u{}^+$
1_u(IV)	1.56	1.60	1 $^3\Sigma_u{}^-$, 2 $^3\Sigma_u{}^+$
2_u(II)	1.62	1.60	1 $^1\Delta_u$, 1,2 $^3\Delta_u$
1_u(V)	1.78	1.84	2 $^3\Pi_u$, 1 $^3\Sigma_u{}^+$, 2 $^5\Pi_u$

[a] The vertical excitation energies are calculated at the Bi−Bi distance of 2.910 Å.

TABLE 5: Low-Lying u-States, to Which Excitations from the $X0_g{}^+$ Ground State Are Dipole-Allowed, Their Leading Configurations, Excitation Energies Δ*E*, Transition Dipole Moments *μ* (LSC−SO−CI), and Oscillator Strengths *f*[a]

state	leading configuration	ΔE/eV	μ/ea_0	f
$X0_g{}^+$	$\sigma_g{}^2\pi_u{}^4\pi_g{}^2$	0		
$0_u{}^+$(I)	$\pi_g \rightarrow \sigma_u$	0.14	1.916	0.013
1_u(I)	$\pi_g \rightarrow \sigma_u$	0.15	1.649	0.010
1_u(II)	$\pi_g \rightarrow \sigma_u$	0.89	0.228	0.001
1_u(III)	$\pi_g \rightarrow \pi_u^*$	1.46	0.216	0.002
$0_u{}^+$(II)	$\pi_g \rightarrow \pi_u^*$	1.47	1.655	0.100
1_u(IV)	$\pi_g \rightarrow \pi_u^*$	1.60	0.252	0.002
1_u(V)	$\pi_u \rightarrow \pi_g$	1.84	0.286	0.004
1_u(VI)	$\pi_u \rightarrow \pi_g$	1.88	0.235	0.003
$0_u{}^+$(III)	$\pi_u \rightarrow \pi_g$	2.09	0.986	0.050
1_u(VIII)	$\sigma_g \rightarrow \sigma_u$	2.21	0.577	0.018
$0_u{}^+$(IV)	$\pi_u \rightarrow \sigma_g^*$	2.24	0.663	0.024
1_u(IX)	$\pi_u \rightarrow \sigma_g^*$, $\pi_u{}^2 \rightarrow \pi_g\sigma_u$	2.25	0.138	0.001
1_u(X)	$\pi_u \rightarrow \pi_g$, $\pi_g \rightarrow \pi_u^*$	2.30	0.126	0.001
$0_u{}^+$(V)	$\sigma_g \rightarrow \sigma_u$	2.39	1.922	0.216
1_u(XI)	$\pi_g \rightarrow \pi_u^*$, $\pi_u \rightarrow \pi_g$	2.44	0.216	0.003
1_u(XII)	$\pi_g{}^2 \rightarrow \pi_u^*\,\sigma_g^*$, $\pi_g \rightarrow \sigma_u^*$	2.54	0.292	0.005
$0_u{}^+$(VI)	$\pi_g \rightarrow \pi_u^*$	2.57	0.626	0.025
1_u(XIII)	$\pi_u \rightarrow \pi_g^*$	2.60	0.231	0.003
$0_u{}^+$(VII)	$\pi_g \rightarrow \sigma_u$	2.66	0.418	0.011
1_u(XVII)	$\pi_u \rightarrow \sigma_g^*$, $\pi_u{}^2 \rightarrow \pi_g^*\,\sigma_u$	2.86	0.133	0.001
$0_u{}^+$(IX)	$\pi_u \rightarrow \pi_g^*$	2.87	0.615	0.027
$1_u{}^+$ (XIII)	$\pi_u \rightarrow \pi_g^*$	2.87	0.329	0.008

[a] Vertical excitation energies are calculated at the Bi−Bi distance of 2.910 Å. Only states with $f \geq 0.001$ are presented.

6.2. Assignment of the Excitation Spectrum. The $0_u{}^+$ and 1_u states up to excitation energies of 2.9 eV are summarized in Table 5 with the associated transition dipole moments (μ) and the oscillator strengths (f). The degeneracy of the 1_u states was taken into account, with μ values defined as $\mu = \sqrt{\mu_x{}^2 + \mu_y{}^2}$. The oscillator strength is related to the transition dipole moment as $f \propto \Delta E\mu^2$, where ΔE is the excitation energy associated with the transition dipole moment. Table 5 also summarizes the orbital character of the leading excitations (from the viewpoint of one-electron orbitals in the absence of spin−orbit coupling). The excitation energies for the states up to 1_u(V) were calculated by the MR−SO−CI method, and those for the higher-lying states by the LSC−SO−CI method.

As already discussed in the previous section, the three lowest u-states of Table 5, 0_u^+(I) and 1_u(I,II), are mainly determined by the $^{1,3}\Pi_u(...\sigma_g^2\pi_u^4\pi_g\sigma_u)$ contributions and thus correspond to the $\pi_g \rightarrow \sigma_u$ excitation (i.e., the $\pi^* \rightarrow \sigma^*$ excitation in the notation of section 5.3). The present relativistic CI calculations show that the three transitions associated with $X0_g^+ \rightarrow 0_u^+$(I), 1_u(I,II) have very small excitation energies, and the transition dipole moments for two of the three are not small. The $X0_g^+ \rightarrow 0_u^+$(I) transition is a parallel one, so it is obvious that this transition cannot be caused by the $\pi^* \rightarrow \sigma^*$ excitation. In this case, an essentially multireference character of the electronic states of Bi_2^{2-} plays a decisive role, which originates from high density of states corresponding to different electronic configurations and very strong spin−orbit interaction among them. The latter induces a notable mixing of the $^{1,3}\Sigma_u^-(...\sigma_g\pi_u^4\pi_g^2\sigma_u)$ and $^3\Sigma_u^-(...\sigma_g^2\pi_u^3\pi_g^3)$ character into the 0_u^+(I) state, which leads to altogether 9.4% of its wave function. The corresponding excitations with respect to the ground state are $\sigma_g \rightarrow \sigma_u$ (i.e., $\sigma \rightarrow \sigma^*$) and $\pi_u \rightarrow \pi_g$ (i.e., $\pi \rightarrow \pi^*$), which are strong as shown in section 5.3.

A situation with the perpendicular $X0_g^+ \rightarrow 1_u$(I) transition is quite different. It is caused by the $\pi^* \rightarrow \sigma^*$ excitation, which according to the analysis of section 5.3 must be weak. However, the present CI calculations show that the σ^* orbital acquires a lot of Rydberg character, which was not taken into account in the DFT treatment. This explains why the perpendicular transition moment is relatively large as well, although somewhat smaller than the parallel one (see Table 5 and note the $\sqrt{2}$ factor accounting for the degeneracy of the 1_u(I) state). The small frequency factors (i.e., the small excitation energies ΔE) of these transitions, however, lead to weak oscillator strengths. Therefore, these transitions cannot account for the experimental UV−vis spectrum of (K-crypt)$_2$Bi$_2$.

The next group of u-states, 0_u^+(II) and 1_u(III,IV), lies in the 1.47−1.60 eV energy range and arises from the $\pi_g \rightarrow \pi_u^*$ excitation. The transition from $X0_g^+$ to one of these states, 0_u^+(II), is characterized by a large transition dipole moment (μ = 1.655 ea$_0$) and $f \approx 0.10$. This type of excitation was not considered in section 5, because the Rydberg-type π_u^* orbital was not considered in the DFT calculations. In the UV−vis spectrum of (K-crypt)$_2$Bi$_2$, a small and very broad hump is observed at ∼1.55 eV (i.e., ∼800 nm). Additional calculations at internuclear separations around the $X0_g^+$ equilibrium distance show that the 0_u^+(II) state has a minimum at a shorter distance (∼2.805 Å), which should lead to a broad absorption due to transitions to various vibrational levels of the upper state. Thus, one might speculate if the observed experimental feature at ∼1.55 eV is related to the $X0_g^+ \rightarrow 0_u^+$(II) transition. However, this assignment is unreasonable, as discussed below.

The next-highest states, 1_u(V,VI) and 0_u^+(III), as well as 1_u(X) lying slightly higher, originate from the $\pi_u \rightarrow \pi_g$ excitation. In terms of the $j-j$ coupling discussed in section 5.3, the $X0_g^+ \rightarrow 0_u^+$(III) excitation corresponds to the $1e_{u3/2} \rightarrow 1e_{g3/2}$ transition, which was predicted to have a large transition dipole moment. The calculated μ value for this transition is indeed fairly large, 0.986 ea$_0$, and it is positioned at 2.09 eV. Thus, one might consider that the $X0_g^+ \rightarrow 0_u^+$(III) excitation leads to the absorption at ∼2.05 eV (Figure 1). In addition, one might suggest that the $X0_g^+ \rightarrow 1_u$(VIII), 0_u^+(IV) transitions can also contribute to this absorption (halfwidth ∼0.25 eV), while the $X0_g^+ \rightarrow 1_u$(V,VI) transitions are partly responsible for the long wavelength tail of this peak. However, this picture has two weak points. First, the $X0_g^+ \rightarrow 0_u^+$(III) transition is too weak (f = 0.050) compared with the $X0_g^+ \rightarrow 0_u^+$(II) excitation to explain the strong absorption around 2.05 eV. Second, there is one more strong transition, $X0_g^+ \rightarrow 0_u^+$(V), which is calculated to lie at 2.39 eV, i.e., almost exactly at the midpoint between the two experimental peaks at 2.05 and 2.85 eV.

The theoretical and experimental spectra of Bi_2^{2-} are best matched by supposing that the calculated excitation energies of the low-lying 0_u^+ states (mainly responsible for the absorption in the observed spectral range) are underestimated by 0.4−0.6 eV. Under this assumption, the $X0_g^+ \rightarrow 0_u^+$(II) transition (with excitation energy of 1.47 eV) is responsible for the strong band at ∼2.05 eV, and the $X0_g^+ \rightarrow 0_u^+$(V) transition (with excitation energy of 2.39 eV) for the strong peak at ∼2.85 eV. The $X0_g^+ \rightarrow 0_u^+$(V) transition has a large transition dipole moment (1.922 ea$_0$) and a large oscillator strength (f = 0.216), because its leading configuration $\sigma \rightarrow \sigma^*$ leads to a large transition dipole moment as discussed in section 5.3. Then, the $X0_g^+ \rightarrow 0_u^+$(III), 1_u(VIII), 0_u^+(IV) excitations should give rise to the nonvanishing absorption in the region between the two absorption peaks. The increase in the absorption intensity at energies higher than 3.3 eV (Figure 1) is probably caused by a large number of relatively weak contributions resulting from a very high density of electronic states in this energy range (for simplicity, this is not shown in Table 5).

There are several possible causes for the above-mentioned underestimation of the excitation energies for the low-lying 0_u^+ states. For example, the energy of the ground state $X0_g^+$ is underestimated, as often found for the MRD-CI methods. In addition, the positions of the calculated maxima in the absorption spectrum can be influenced by the shifting of the potential energy curves of the excited states with respect to that of the ground state, and also by the dependence of the transition dipole moment on the internuclear distance. It should also be recalled that the Bi_2^{2-} dianion of (K-crypt)$_2$Bi$_2$ present in ethylenediamine solution is not identical to an isolated free Bi_2^{2-} dianion in vacuum.

The relativistic DFT calculations are far less adequate than are the relativistic CI calculations for the analysis of the UV/vis spectrum of Bi_2^{2-}. For example, the $X0_g^+ \rightarrow 0_u^+$(II) excitation, which is responsible for the strong absorption at ∼2.05 eV and whose leading configuration is $\pi_g \rightarrow \pi_u^*$, is not described because the relativistic DFT calculations do not take into consideration Rydberg-type orbitals such as π_u^*. A strong admixture of Rydberg character to the σ_u (i.e., σ^*) orbital also causes an increase in the $X0_g^+ \rightarrow 1_u$(I) transition moment in comparison with the DFT analysis. For the low-energy parallel transition, $X0_g^+ \rightarrow 0_u^+$(I), an essentially multireference character of the upper state leads to a fairly strong transition moment. The primary reason for the shortcoming of the DFT method in this case is that it is based on a single-determinant wave function, so electronic excitations are described as transitions between occupied and unoccupied one-electron orbitals. In principle, DFT calculations can provide more accurate estimates of excitation energies when multideterminant wave functions are used to describe electronic excitations.[41−43]

7. Concluding Remarks

Our relativistic DFT calculations for the isoelectronic diatomic dianions Q_2^{2-} (Q = N, P, As, Sb, Bi) show that the closed-shell state $(2e_{g1/2})^2(1e_{g3/2})^0$ is more stable than the open-shell state $(2e_{g1/2})^1(1e_{g3/2})^1$ for Bi_2^{2-}, while the opposite is the case for N_2^{2-}, P_2^{2-}, As_2^{2-}, and Sb_2^{2-}. This explains why, unlike paramagnetic O_2, the Bi_2^{2-} anions of (K-crypt)$_2$Bi$_2$ are diamagnetic and EPR-silent. Our relativistic CI calculations suggest that the $X0_g^+ \rightarrow 0_u^+$(II) transition is responsible for the strong peak around 2.05 eV, and the $X0_g^+ \rightarrow 0_u^+$(V) transition for the strong peak at ∼2.85 eV. The nonvanishing absorption in the region between the two peaks is probably caused by the $X0_g^+ \rightarrow 0_u^+$(III), 1_u(VIII), and 0_u^+(IV) transitions and an increase in the absorption intensity at energies higher than 3.3 eV by a large number of relatively weak contributions from a very high density of electronic states in this energy range.

Acknowledgment. This work was supported by the Office of Basic Energy Sciences, Division of Materials Sciences, U.S. Department of Energy, under Grant DE-FG02-86ER45259 and by the National Science Foundation under grant CHE-0098004.

References and Notes

(1) Xu, L.; Bobev, S.; El-Bahraoui, J.; Sevov, S. C. *J. Am. Chem. Soc.* **2000**, *122*, 1838.

(2) Gascoin, F.; Sevov, S. C. *J. Am. Chem. Soc.* **2000**, *122*, 10251.

(3) Powell, R. E. *J. Chem. Ed.* **1969**, *45*, 558.

(4) Pitzer, K. S. *Acc. Chem. Res.* **1979**, *12*, 271.

(5) Pyykkö, P.; Desclaux, J.-P. *Acc. Chem. Res.* **1979**, *12*, 276.

(6) Ziegler, T.; Snijders, J. G.; Baerends, E. J. *J. Chem. Phys.* **1981**, *74*, 1271.

(7) Ziegler, T.; Tschinke, V.; Baerends, E. J.; Snijders, J. G.; Ravenek, W. *J. Phys. Chem.* **1989**, *93*, 3050.

(8) Pyykkö, P. *Chem. Rev.* **1988**, *88*, 563.

(9) Pepper, M.; Bursten, B. E. *Chem. Rev.* **1991**, *91*, 719.

(10) Kutzelnigg, W. *Chem. Phys.* **1997**, *225*, 203.

(11) (a) Balasubramanian, K. *Relativistic Effects in Chemistry: Part A, Theory and Techniques*, John Wiley: New York, 1997. (b) Balasubramanian, K. *Relativistic Effects in Chemistry: Part B, Applications*, John Wiley: New York, 1997.

(12) Pyykkö, P. *Relativistic Theory of Atoms and Molecules I−III*, Springer-Verlag: Berlin, 1986, 1993, 2000.

(13) Autschbach, J.; Ziegler, T. *J. Chem. Phys.* **2000**, *113*, 936.

(14) Christiansen, P. A. *Chem. Phys. Lett.* **1984**, *109*, 145.

(15) Balasubramanian, K.; Liao, D.-W. *J. Chem. Phys.* **1991**, *95*, 3064.

(16) Das, K. K.; Liebermann, H.-P.; Buenker, R. J.; Hirsch, G. *J. Chem. Phys.* **1995**, *102*, 4518.

(17) van Lenthe, E.; Snijders, J. G.; Baerends, E. J. *J. Chem. Phys.* **1996**, *105*, 6505.

(18) Varga, S.; Fricke, B. Nakamatsu, H.; Mukoyama, T.; Anton, J.; Geschke, D.; Heitmann, A.; Engel, E.; Baştuğ, T. *J. Chem. Phys.* **2000**, *112*, 3499.

(19) Matveev, A.; Rösch, N. *J. Chem. Phys.* **2003**, *118*, 3997.

(20) Choi, Y. J.; Lee, Y. S.; *J. Chem. Phys.* **2003**, *119*, 2014.

(21) Kim, Y. S.; Lee, Y. S. *J. Chem. Phys.* **2003**, *119*, 12169.

(22) Liu, W.; Hong, G.; Dai, D.; Li, L.; Dolg, M. *Theor. Chem. Acct.* **1997**, *96*, 75.

(23) Liu, W.; Wang, F.; Li, L. *J. Theor. Comput. Chem.* **2003**, *2*, 257, and the references therein.

(24) Becke, A. D. *Phys. Rev. A* **1988**, *38*, 3098.

(25) Perdew, J. P. *Phys. Rev. B* **1986**, *33*, 8822.

(26) Wildman, S. A.; DiLabio, G. A.; Christiansen, P. A. *J. Chem. Phys.* **1987**, *107*, 9975.

(27) Buenker, R. J.; Alekseyev, A. B.; Liebermann, H.-P.; Lingott, R.; Hirsch, G. *J. Chem. Phys.* **1998**, *108*, 3400.

(28) Alekseyev, A. B.; Liebermann, H.-P.; Buenker, R. J. In *Recent Advances in Relativistic Molecular Theory*; Hirao, K., Ishikawa, Y., Eds.; World Scientific: Singapore, 2004; p 65.

(29) (a) Buenker, R. J.; Peyerimhoff, S. D. *Theor. Chim. Acta* **1974**, *35*, 33. Buenker, R. J.; Peyerimhoff, S. D. *Theor. Chim. Acta* **1975**, *39*, 217. (b) Buenker, R. J.; Peyerimhoff, S. D.; Butscher, W. *Mol. Phys.* **1978**, *35*, 771.

(30) Krebs, S.; Buenker, R. J. *J. Chem. Phys.* **1995**, *103*, 5613.

(31) Krebs, S.; Buenker, R. J. In *Recent Advances in Multireference Methods*; Hirao, K., Ed.; World Scientific: Singapore, 1999; p 1.

(32) Davidson, E. R. In *The World of Quantum Chemistry*; Daudel, R., Pullman, B., Eds.; Reidel: Dordrecht, 1974; p 17.

(33) (a) Hirsch, G.; Bruna, P. J.; Peyerimhoff, S. D. Buenker, R. J. *Chem. Phys. Lett.* **1977**, *52*, 442. (b) Knowles, D. B.; Alvarez-Collado, J. R.; Hirsch, G.; Buenker, R. J. *J. Chem. Phys.* **1990**, *92*, 585.

(34) Whangbo, M.-H. *J. Chem. Phys.* **1979**, *70*, 4963.

(35) In principle one could take more electrons (e.g., 5s and 5p electrons) out of the core to prove this point computationally. Such calculations were not carried out because an important goal of our work is to describe the excited states and absorption of Bi_2^{2-}, which makes it unreasonable to consider more valence electrons. Furthermore, even if there is a small systematic overestimation of the Bi−Bi bond length, it should be more or less the same for all states so that the overestimation of the Bi−Bi bond length is not really important for electronic transitions.

(36) Slater, J. C. *Adv. Quantum Chem.* **1972**, *6*, 1.

(37) Dai, D.; Whangbo, M.-H. *J. Chem. Phys.* **2001**, *114*, 2887.

(38) For the generalization of Slater's original transition-state concept and its applications to a core electron binding energy calculation, see: Cavigliasso, G.; Chong, D. *J. Chem. Phys.* **1999**, *111*, 9485, and the references therein.

(39) Here the superscripts + and − for an $\Omega = 0$ state mean that the wave function is respectively symmetric and antisymmetric with respect to the mirror plane of symmetry that goes through the molecular axis. This symmetry element does not exist for the $\Omega \neq 0$ states.

(40) Our calculations for Bi_2^{2-} were carried out by employing the SAMOA (Structure and Molecular Orbital Analyzer) program package (Dai, D.; Ren, J.; Liang, W.; Whangbo, M.-H., http://chvamw.chem.ncsu.edu/, 2002). Our calculations used the Bi−Bi bond length of 3 Å and the double-ζ Slater type orbitals for the Bi 6p orbitals (Clementi, E.; Roetti, C., *Atomic Data Nuclear Data Tables* **1974**, *14*, 177). To be consistent with our discussion based solely on the Bi 6p orbitals, the Bi 6s orbitals were omitted from our calculations. However, the inclusion of these orbitals does not change our conclusion.

(41) Stoll, H. *Chem. Phys. Lett.* **2003**, *376*, 141.

(42) Filatov, M.; Shaik, S. *J. Chem. Phys.* **1999**, *110*, 116.

(43) Daul, C.; Güdel, H.-U.; Weber, J. *J. Chem. Phys.* **1993**, *98*, 4023.